University of Nebraska - Lincoln

DigitalCommons@University of Nebraska - Lincoln

Faculty Publications from the Department of Electrical and Computer Engineering

Electrical & Computer Engineering, Department of

Graphene on Pt(111): Growth and substrate interaction

Peter Sutter
Brookhaven National Laboratory, psutter@unl.edu

Jerzy T. Sadowski
Brookhaven National Laboratory

Eli Sutter
Brookhaven National Laboratory, esutter@unl.edu

Graphene on Pt(111): Growth and substrate interaction

Peter Sutter, Jerzy T. Sadowski, and Eli Sutter

Center for Functional Nanomaterials, Brookhaven National Laboratory, Upton, New York 11973, USA

In situ low-energy electron microscopy (LEEM) of graphene growth combined with measurements of the graphene structure and electronic band structure has been used to study graphene on Pt(111). Growth by carbon segregation produces macroscopic monolayer graphene domains extending continuously across Pt(111) substrate steps and bounded by strongly faceted edges. LEEM during cooling from the growth temperature shows the propagation of wrinkles in the graphene sheet, driven by thermal stress. The lattice mismatch between graphene and Pt(111) is accommodated by moiré structures with a large number of different rotational variants, without a clear preference for a particular interface geometry. Fast and slow growing graphene domains exhibit moiré structures with small [e.g., $(3\times3)_G$, $(\sqrt{6}\times\sqrt{6})R2_G$, and $(2\times2)R4_G$] and large unit cells [e.g., $(\sqrt{44}\times\sqrt{44})R15_G$, $(\sqrt{52}\times\sqrt{52})R14_G$, and $(8\times8)_G$], respectively. A weak substrate coupling, suggested by the growth and structural properties of monolayer graphene on Pt(111), is confirmed by maps of the band structure, which is close to that of isolated graphene aside from minimal hole doping due to charge transfer from the metal. Finally, the decoupled graphene monolayer on Pt(111) appears impenetrable to carbon diffusion, which self-limits the graphene growth at monolayer thickness. Thicker graphene domains, which can form at boundaries between monolayer domains, have been used to characterize the properties of few-layer graphene on Pt(111).

I. INTRODUCTION

Graphene, a two-dimensional sp^2 bonded honeycomb lattice of carbon atoms, has shown remarkable properties that are being investigated actively in basic research[1] and which make it a promising material for a number of applications, e.g., in microelectronics,[2,3] large-area optoelectronics,[4] or in sensors[5] and actuators.[6] To realize such potential applications, reliable methods for large-scale graphene synthesis are required. Graphene synthesis by epitaxy on noncarbide forming transition metals[7,8] has been considered recently as a scalable alternative to micromechanical cleavage. If the growth is performed on metal foils or thin films, such metal catalyzed graphene sheets can be isolated by etching away the substrate and transferred to a suitable support material.[9,10]

Graphene synthesis has recently been performed successfully on a number of transition metals, including Ni,[9–12] Ru,[7,13] Ir,[8] and Cu.[14] However, the study of graphene [or "monolayer (ML) graphite"] on transition metals dates back much longer.[15,16] In particular, the formation and properties of monolayer graphite on Pt have been studied early on[17] since Pt and Pt alloys are used widely for hydrocarbon catalysis, where the formation of graphitic surface structures represents an unwanted by-product that can poison the active phase of the catalyst. Recent x-ray absorption measurements have suggested that ML graphene on Pt stands out as the system with the weakest graphene-metal interaction among a broader group of 3d, 4d, and 5d transition metals.[18] While monolayer graphene on Ru(0001) and Ni(111) couples strongly to the metal substrate, other metals such as Ir and Cu show a much weaker (van der Waals) interfacial interaction with graphene. Previous observations, using both diffraction[17,19] and imaging,[20–23] of coexisting rotational domains and the formation of different interfacial moiré structures for graphene on Pt(111) support the notion of a weak interfacial interaction, similar to graphene on Ir(111).[24] It can be expected that the weak substrate coupling will affect the growth mechanisms, structural, and electronic properties of graphene on Pt and may cause these properties to be distinct from other transition metal supported graphene systems.

Here we use *in situ* low-energy electron microscopy (LEEM) to probe the growth, structure, and electronic properties of graphene on Pt(111). In contrast to previous studies, which have been based on off-line graphene growth followed either by high-resolution imaging of randomly chosen microscopic surface regions or by averaging measurements (diffraction, x-ray absorption, and photoelectron spectroscopy) on macroscopic sample areas, we combine direct real-time observations of graphene growth with the probing of different properties in selected microscopic sample areas. In this way, we are able to correlate the growth, structure, separation from the metal substrate, and electronic band structure for ML graphene domains on Pt(111) with specific interfacial motifs, and to explore possible mechanisms leading to the growth of few-layer graphene beyond 1 ML thickness.

II. EXPERIMENT

Graphene epitaxy was performed on a Pt(111) single crystal, enriched with interstitial carbon by hydrocarbon (ethylene) exposure at temperatures above 1000 °C. A slow lowering of the sample temperature reduces the carbon solubility in the metal[25] and causes carbon surface segregation, which in turn drives graphene growth.[7] We observed the growth of initial ML graphene islands, their coalescence, and possible mechanisms for the growth of thicker (few-layer) graphene domains in real time by bright-field LEEM. The physical and electronic properties of the as-grown graphene were deter-

mined *in situ* by complementary measurements in the LEEM instrument. Selected-area low-energy electron diffraction (micro-LEED) on small sample areas (2 μm diameter) was used to establish the structure and substrate registry of the graphene layers. Intensity-voltage measurements, both in real space (*IV* LEEM) (Ref. 26) and reciprocal space (*IV* LEED), were combined with dynamical multiple-scattering calculations of the low-energy electron reflectivity[27] to determine the layer spacing between ML graphene and the metal substrate, and to probe the interlayer spacing in few-layer graphene domains. The electronic structure of ML graphene on Pt(111) was mapped at room temperature *in situ* in the LEEM instrument by collecting angle-resolved photoelectron spectra from micron-sized sample areas (micro-ARPES). Ultraviolet synchrotron-radiation (energy $h\nu = 42$ eV; beamline U5UA at the National Synchrotron Light Source)[28] incident perpendicular to the sample was used to excite photoelectrons, which were energy filtered by an imaging energy analyzer (energy resolution <0.3 eV) and whose angular distribution was mapped in reciprocal space using the electron optics and detector system of the LEEM. The raw data comprised photoelectron angular distributions beyond the first Brillouin zone (BZ) for energies from -18 to $+2$ eV relative to E_F in increments of 0.1 eV. Projections along high-symmetry directions in reciprocal space were used to generate band-structure maps along those directions.

III. GROWTH AND SUBSTRATE INTERACTION OF MONOLAYER GRAPHENE ON Pt(111)

The nucleation and growth of a representative monocrystalline ML graphene domain by carbon surface segregation, initiated by slow cooling from 1000 °C, is shown in Fig. 1. At high temperatures (here $T = 864$ °C), the graphene nucleation is sparse and adjacent nuclei are usually spaced well over 100 μm apart. Such sparse nucleation is achieved by carefully controlling the supersaturation of carbon at the surface, i.e., using slow temperature ramps to induce the controlled segregation of carbon from the bulk. Following the initial nucleation, each graphene domain rapidly expands by attachment of C to the edges to reach a size of several tens of micrometer in about 1 min. This growth by edge attachment occurs continuously, i.e., without secondary nucleation events, to produce single-crystalline graphene domains whose sizes exceed the average step spacing on the Pt(111) crystal by about two orders of magnitude, thus demonstrating a continuous, carpetlike flow of the graphene sheet across substrate steps, similar to graphene growth on Ru (0001) (Ref. 7) and Ir(111).[29] The domain boundaries are straight over macroscopic distances. Adjacent straight edge segments meet mostly under angles of 60° and 120°, or 90° and 150°, consistent with zigzag/zigzag, armchair/armchair, and zigzag/armchair intersections but angles of 45° and 135° are also observed. It is plausible to assign the majority of the macroscopically long straight segments to zigzag and armchair graphene edges [black and white lines in Fig. 1(d)], and the edges intersecting at 45° and 135° angles to mixed edge terminations containing regular arrays of kinks [gray lines in Fig. 1(d)]. However, it is also possible that the observed
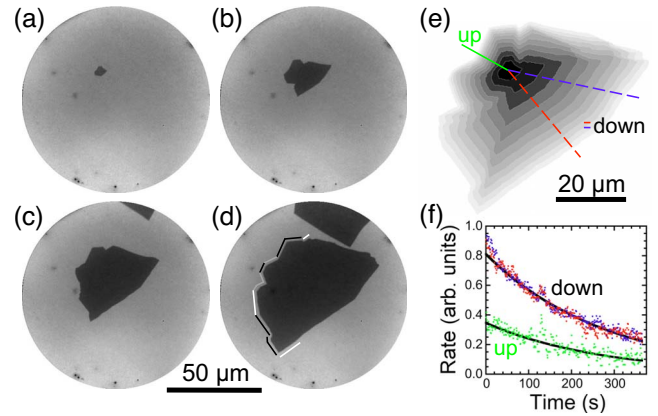

FIG. 1. (Color online) Monolayer graphene growth on Pt(111). [(a)–(d)] Sequence of LEEM images obtained during growth of a single-crystalline ML graphene domain by carbon surface segregation at constant $T = 864$ °C. Elapsed time [relative to frame (a)]: (b) -30 s; (c) -90 s; and (d) -190 s. Black and white lines in (d) delineate majority and minority edges, respectively. (e) Domain edge contours at constant time intervals of 6 s, illustrating the growth rates in different in-plane directions aligned with the uphill and downhill directions of the stepped substrate. (f) Graphene growth rates along the lines shown in (e). Solid lines are exponential fits, a·exp(−t/τ), with a universal decay time $\tau = 280$ s for all curves.

straight edges are low-energy facets consisting of different types of edge segments at the atomic scale. To resolve this question, additional experiments are needed using microscopic techniques with higher spatial resolution than LEEM.

Figures 1(e) and 1(f) show an analysis of the linear growth rate for directions approximately perpendicular to the Pt(111) substrate steps. The analysis shows growth rates across substrate steps in the uphill (solid green) and downhill (dashed red, blue) directions differing by about a factor of 2. For both directions, the growth at constant temperature ($T = 864$ °C) gradually decreases, following an exponential dependence with time constant $\tau = 280$ s. Since the growth occurs by carbon segregation from the Pt bulk, this characteristic time represents the decrease in the density of surface carbon due to the depletion of the reservoir of interstitial carbon in the metal substrate.

It is instructive to contrast the growth characteristics of ML graphene on Pt(111) with those observed on Ru(0001). Epitaxial graphene on Ru forms a moiré structure characterized by a strong chemical interaction with the metal substrate,[30–32] which leads to a well-defined epitaxial relationship with closely aligned crystal axes of the substrate and graphene lattices, and affects the graphene domain growth in two ways: orbital overlap at steps almost completely suppresses the growth across substrate steps in the uphill direction; hence, one edge of the graphene domain traces the pinning substrate step. In all other directions, the rate of carbon incorporation is nearly isotropic, i.e., at sufficiently early growth stages the resulting edge of the graphene domain approximates a semicircle. The difference in growth rate between the uphill and downhill directions is very large, with the ratio of the two rates reaching values of 100 or more.[7] Conversely, for ML graphene growth on Pt(111), a small

growth rate anisotropy due to substrate steps [similar to that observed for Ir(111) (Ref. 33)] indicates a very minor effect of the metal substrate, suggesting that the interaction between graphene and the Pt substrate is weak. The macroscopically long, straight boundaries of the graphene domains are consistent with this conclusion.

As the sample cools down from typical growth temperatures of about 800 °C, where the epitaxial relationship between graphene and substrate is defined, the mismatch in thermal-expansion coefficients between Pt ($\sim$8.8 $\times 10^{-6}$ K^{-1}) and graphene ($<1 \times 10^{-6}$ K^{-1}) leads to a progressive buildup of compressive stress in the graphene sheet. It has been shown previously that such stress can be relaxed elastically (i.e., without formation of crystal defects in the graphene) by the formation of wrinkles,[24,34–36] long-range linear ridges in which the intact graphene sheet is locally warped up and decouples from the substrate, thus relaxing some of the compression in the graphene. Figure 2(a) shows a typical wrinkle network on ML graphene on Pt(111) after cooling to room temperature. Generally, one set of wrinkles aligns with the predominant direction of the atomic steps of the Pt(111) substrate [approximately horizontal in Fig. 2(a)]. In many instances, individual wrinkles closely follow and meander with a substrate step over micrometer distances. A second set of wrinkles runs perpendicular to the first set, presumably ensuring that both components of the biaxial thermal stress are relaxed. Although local deviations from these predominant directions are observed, there is no clear correlation between the direction of the wrinkles and the sixfold symmetry of the substrate or graphene lattices. Individual wrinkles can end inside a pristine part of the graphene domain, i.e., do not necessarily form a fully interconnected network.

The overall morphology of the network in Fig. 2(a) can be understood by considering the wrinkle formation mechanism. The gain in elastic energy, due to the stress relaxation achieved by generating a wrinkle, is offset in part by the energy cost of detaching a narrow linear strip of graphene from the metal substrate. It is reasonable to expect that this process occurs gradually, i.e., that the wrinkle propagates by progressively detaching graphene from the substrate at the wrinkle tip—analogous to the opposite process, the rupturing of a two-dimensional sheet under tension.[38] The detachment should be easiest along step edges, where the coupling to the substrate is weak. Indeed, we observe the onset of wrinkle formation parallel to substrate steps. However, since the steps are aligned roughly parallel, only one component of the biaxial thermal compression is effectively relaxed by wrinkles along steps. To achieve biaxial relaxation, additional wrinkles need to form perpendicular to the step direction. These wrinkles will likely propagate more slowly and may get pinned by point defects or impurities in the substrate or the graphene sheet itself, and hence end without connecting to other wrinkles, as is indeed observed in Fig. 2(a).

To verify the above scenario, we designed *in situ* microscopy experiments that directly show the propagation of wrinkles on ML graphene on Pt(111). Graphene was grown in the LEEM instrument at about 800 °C, followed by slow cooling. To limit the buildup of compressive thermal stress, i.e., the driving force for wrinkle formation, the cooling was
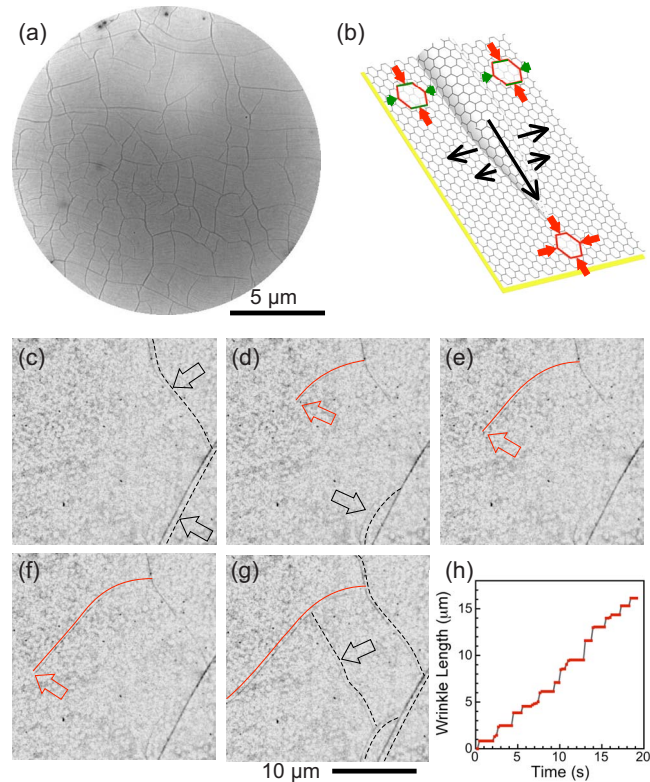

FIG. 2. (Color online) Relaxation of thermal stress by formation of wrinkle networks. (a) LEEM image of ML graphene on Pt(111) after cooling from a growth temperature of 800 °C to room temperature. Faint wavy lines along the horizontal direction are atomic steps on the Pt(111) surface, accommodated by the continuous graphene layer in a carpetlike fashion. Darker horizontal and vertical lines reflect a network of wrinkles in the graphene sheet. (b) Schematic drawing of a wrinkle tip, illustrating the biaxial compression before and uniaxial relaxation after the passage of the wrinkle. Black arrows indicate the direction of propagation, as well as the progressive lateral growth of the wrinkle. [(c)–(g)] Sequence of LEEM images obtained during cooling at $T = 530$ °C. Dashed (black) lines trace graphene "wrinkles." Solid (red) lines mark one propagating wrinkle. Rolling ball background subtraction has been applied to these images (Ref. 37). The speckled contrast is due to the microchannelplate detector. (h) Measured lengthening of the wrinkle marked in (c)–(g).

interrupted and the temperature stabilized as soon as the first wrinkles developed. Images from the LEEM movie of the further evolution of the graphene sheet are shown in Figs. 2(b)–2(g). Initially, two wrinkles in orthogonal directions are visible in the field of view (black dashed lines). The local wrinkle density is below that required to relax the thermal stress due to the partial cooling [compare to Fig. 2(a)]. Further wrinkles appear during observation of this sample area. The formation of one of these wrinkles (solid red lines) progresses sufficiently slowly that it can be imaged by LEEM. The new wrinkle is formed by branching off an existing one and then extends into an area initially covered by flat graphene. The LEEM contrast, due to electron scattering by the slanted side walls of the wrinkles, gradually becomes stronger, which indicates that the detachment and warping of

the graphene sheet continues to grow after the initial formation of a wrinkle [Fig. 2(g)]. A measurement of the time-dependent extension of the wrinkle, finally, shows that the propagation is not continuous but occurs in bursts, interrupted by extended periods without any measurable movement [Fig. 2(h)].

Stress relaxation by wrinkle formation in graphene grown on transition metals appears to be a general phenomenon, which has been observed in several systems including ML graphene on Ni,[34] Ir,[24,36] and Cu.[14] Although it is not yet clear if the wrinkles still exist after the dissolution of the metal and the transfer of the graphene sheet to a different substrate, it would be useful if their formation could be controlled. The observation of kinetic limitations of the wrinkle formation process—the alignment of wrinkles with substrate steps and the expansion in individual bursts—suggests that such control may indeed be possible, e.g., by the judicious definition of arrays of step bunches via lithographic patterning, which could then serve as lines of preferred wrinkle formation by facilitating the detachment of graphene from the substrate.

To determine the interfacial motifs resulting from the formation of ML graphene on a weakly interacting transition metal, such as Pt(111), we performed microdiffraction on single graphene domains. Previous studies on the formation of ML graphene on Pt(111), either employing low-temperature adsorption of ethylene followed by high-temperature annealing[20–23] or the dissociation of a hydrocarbon precursor (methane[39] and propene[18]) at high temperature, identified rotational disorder due to graphene nuclei bonding to the metal substrate in a range of possible moiré structures. Such disorder can be expected in particular for weakly coupled systems, for which the energy landscape is shallow and none of the possible coincidence structures give rise to a clear global minimum in energy. When ML graphene is grown by carbon segregation at controlled low supersaturation, i.e., close to thermodynamic equilibrium, two distinct families of interfacial structures form, as shown by representative single graphene domain micro-LEED patterns in Fig. 3. Following growth to partial surface coverage (total graphene coverage below 1 ML), large graphene domains with sizes exceeding 50 μm, as shown in Fig. 1, invariably exhibit moiré structures with small unit cells, such as the $(3 \times 3)_G$ superstructure in Fig. 3(a). Other structures occurring in large graphene domains included ($\sqrt{6} \times \sqrt{6}$)R2$_G$ and (2×2)R4$_G$. Smaller graphene nuclei (~ 10 μm) grown during the same time period, on the other hand, form a range of large unit-cell coincidence structures, including ($\sqrt{44} \times \sqrt{44}$)R15$_G$ [Fig. 3(b)], ($\sqrt{52} \times \sqrt{52}$)R14$_G$, and $(8 \times 8)_G$. The grouping into two distinct families of interface structures as well as most of the individual moirés listed above have not been reported previously. There are several possible explanations for the observed correlation between the interfacial structure of ML graphene on Pt(111) and the size of the resulting graphene domains. *In situ* LEEM movies of the growth process show that both types of structures nucleate simultaneously, i.e., there is no significant difference in nucleation rate of graphene domains with different interfacial alignment. Instead, we observe different growth rates for domains with large and small-cell moirés, suggest-
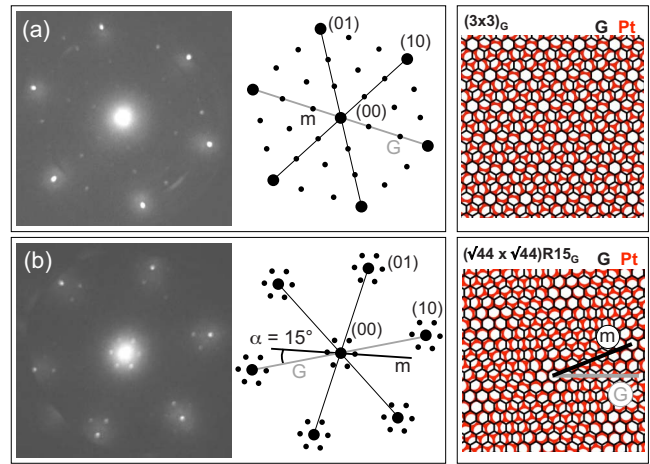

FIG. 3. (Color online) Single-domain micro-LEED patterns of ML graphene on Pt(111). (a) Graphene/Pt(111) moiré with (3×3) periodicity relative to the graphene lattice (graphene under 0.60% compression). (b) Moiré structure with larger ($\sqrt{44} \times \sqrt{44}$) unit cell, relative to graphene (graphene under 0.60% tension). Panels on the right show schematics of both superstructures.

ing that kinetic factors, such as a lower attachment barrier, may cause the faster growth of the domains with small moiré unit cells. Generally, the existence of well-defined moiré coincidence structures with nonvanishing lattice mismatch (Fig. 3) demonstrates that the interaction between the graphene layer and the metal substrate, albeit much weaker than for Ru,[31,40] for example, is still sufficiently strong to strain the graphene lattice and achieve a well-defined epitaxial relationship with the substrate at growth temperatures between 650 and 900 °C (i.e., kT of 80–100 meV). Another weakly interacting system, graphene on Ir(111), has shown a similar variety of moirés, with four distinct structures identified to date.[24] However, while a particular moiré with aligned $[1\bar{1}0]$ and $[11\bar{2}0]$ axes of Ir and graphene, respectively, appears to be predominant on Ir(111),[41] our experiments show no clear preference for any "majority" structure for graphene on Pt(111).

The metal-graphene interaction is closely linked to the interface structure and, in particular, determines the spacing between ML graphene and the Pt(111) surface atoms. We determined this separation by intensity-voltage measurements in reciprocal space (*IV* LEED) or in real space (*IV* LEEM), and comparison of the experimental spectra with dynamical multiple-scattering calculations of the scattered intensity. A previous *IV*-LEED study of ML graphene on Pt(111) has found an unusually large graphene-metal spacing of 3.70 Å, explained by the formation of a closely coupled "carbidic" interlayer with partial carbon coverage in Pt(111) hollow sites between metal and graphene (1.25 Å from the metal surface), and a spacing of 2.45 Å between this carbidic structure and the supported graphene sheet.[19] To date, no other system of graphene on transition metal (Ni, Cu, Rh, Ru, and Ir) has shown signatures of the formation of such carbidic interlayers. Hence, we have used a micro-LEED *IV* analysis on individual, large graphene domains to determine
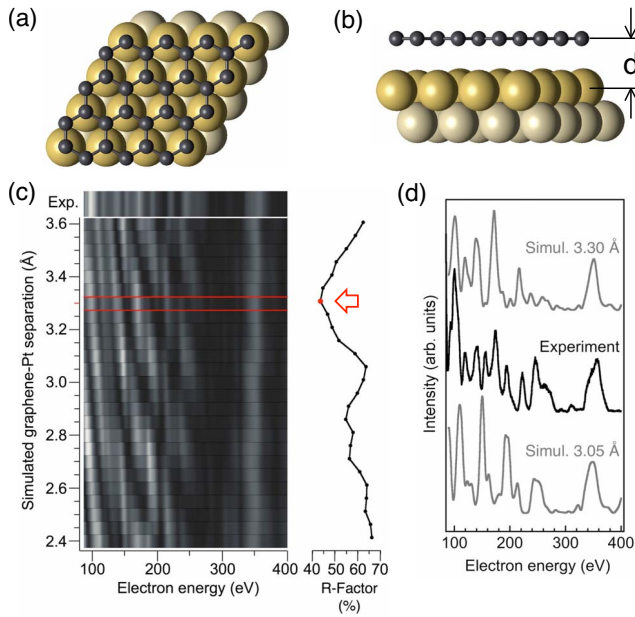
FIG. 4. (Color online) Single graphene domain specular beam *IV* LEED. (a) Top view, (b) side view of the commensurate structure of ML graphene on Pt(111) used for the *IV* simulations. (c) Gray-scale plot comparing the experimental *IV* characteristics ("Exp.") with simulated *IV* spectra [using the geometry shown in (a) and (b)] for graphene/Pt(111) with graphene-metal separation between 2.4 and 3.7 Å. Bright bands correspond to peaks with high reflected intensity, dark areas indicate low reflectivity. Note the systematic shifts of the low-energy peaks (<250 eV) in the simulations with change in graphene-Pt spacing. The side panel gives the corresponding Pendry R factors. The simulation that shows the best agreement with experiment (graphene-Pt separation: $d=3.30$ Å) is marked by an arrow. (d) Direct comparison of the experimental *IV* characteristics on a $(\sqrt{44} \times \sqrt{44})R15_G$ moiré structure with two simulated spectra, one showing the best match, the other matching poorly.

the layer spacing in our samples and re-examine the issue of the interfacial structure and spacing for graphene on Pt(111).

Specular beam (00) *IV* characteristics, which are particularly sensitive to the out-of-plane stacking, were measured on single graphene domains for electron energies ranging from 80 to 400 eV. Simulations, using the TENSERLEED package,[27] were carried out for commensurate graphene structures as shown schematically in Figs. 4(a) and 4(b). To limit the computational complexity and to focus on the graphene/Pt separation, the simulations were performed for a commensurate structure with a small unit cell, comprising a planar, strained graphene layer with one carbon sublattice aligned with surface Pt atoms. An alternative interface geometry, with both carbon sublattices in Pt hollow sites, generally gave poorer agreement with the experimental *IV* characteristics. No fitting of any structural parameters was performed and the only free parameter in the LEED *IV* calculations was the graphene/Pt(111) interlayer spacing, *d*.

Figure 4(c) shows a comparison of the experimental (00) *IV* characteristic of a graphene domain with $(\sqrt{44} \times \sqrt{44})R15_G$ moiré structure, whose diffraction pattern is given in Fig. 3(b), with simulations for a wide range of graphene-metal spacings, 2.4 Å $\leq d \leq$ 3.7 Å. Since the calculation was restricted to a simplified geometry of the graphene/Pt(111) system and no fitting was performed, the Pendry R factors quantifying the match between experiment and simulation are, in general, relatively high. Nevertheless, some clear trends can be observed in comparing experiment and simulation. The location of the most prominent peak at high electron energy (~350 eV) is nearly unaffected by changes in the layer spacing *d*, suggesting that this feature is defined by the reflectivity of the Pt substrate. The *IV* maxima at lower electron energy (<250 eV), on the other hand, are sensitive to the graphene-Pt separation and show systematic shifts as *d* is varied in the simulations. The correspondence between the measured and simulated *IV* characteristics is primarily determined by the location of these peaks.

Varying the ML graphene-Pt separation over a wide interval, the concerted shifts of the lower-energy reflectivity maxima leads to a clear global minimum in the R factor for a spacing $d=3.30$ Å. For this separation, the experimental and simulated *IV* characteristics agree quite well overall (R factor $\sim40\%$), as shown in Fig. 4(d). Since the simulated spectra for 3.25 and 3.35 Å separation already show significant deviations from the experimental data (R factors of 46.7% and 44.7%, respectively), we conclude a graphene/Pt(111) separation of $(3.30 \pm 0.05$ Å) within our structure model. The separation identified here, close to the interlayer spacing in graphite (3.36 Å), suggests that the coupling between graphene and metal is similar to a pure van der Waals interaction. The experimental layer separation determined here is in excellent agreement with a recent density-functional theory (DFT) calculation in the local-density approximation for ML graphene on Pt(111), which has predicted an equilibrium spacing $d_{DFT}=3.30$ Å.[42] In view of the uncertainties of DFT for weakly bound systems and the assumptions of the calculation—a commensurate structure, assuming relaxed graphene matched to in-plane compressively strained Pt(111)—the perfect agreement with our measured spacing may be fortuitous. Nevertheless, the comparison shows that the spacing identified here is very close to that expected for a simple graphene/Pt(111) interface. While our analysis of the experimental single-domain LEED *IV* characteristics with *IV* simulations using a restricted model may be insufficient to identify the detailed structure of ML graphene on Pt(111), the good match obtained for a structure without intercalated carbon for a physically meaningful value of *d* nevertheless casts significant doubt on the previous assumption of an additional carbidic interlayer between metal and graphene for this system.[43]

We have performed a similar *IV* analysis for bilayer graphene domains on Pt(111) (for growth of the bilayer, see below), again assuming a commensurate structure with the interfacial graphene sheet in the arrangement shown in Fig. 4(a) and Bernal stacking of the two graphene layers. Varying the graphene-Pt and graphene-graphene spacings in the simulation, a best match with the experiment (R factor $\sim38\%$) is obtained for a separation between the metal and the interfacial graphene layer of $(3.30 \pm 0.05$ Å), identical to the value for the monolayer, and a separation between the two graphene sheets equal to the interlayer spacing in graphite.
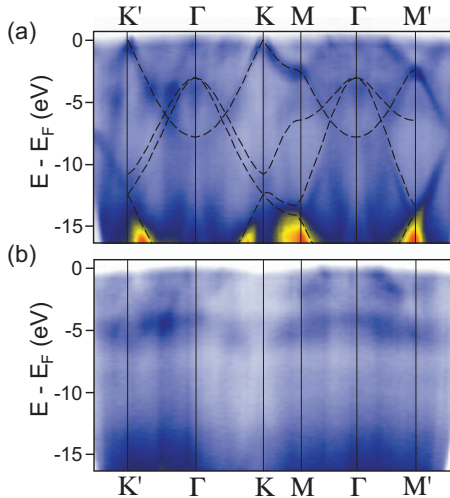
FIG. 5. (Color) Micro-ARPES band-structure maps. (a) Overview spectrum of ML graphene on Pt(111) along high-symmetry directions in the first Brillouin zone. Dashed lines: scaled density-functional theory computed bands of free-standing graphene (Ref. 45). (b) Reference spectrum of the Pt(111) substrate between ML graphene domains, along the same reciprocal space trajectory as (a).
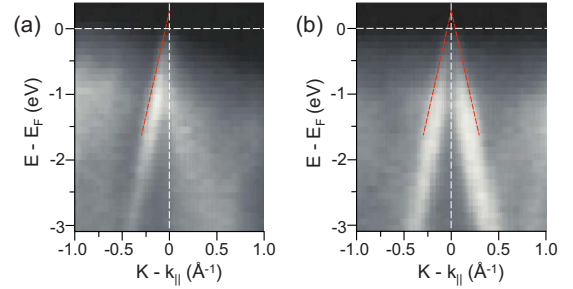

FIG. 6. (Color online) Close-up micro-ARPES spectra near the K point of the graphene Brillouin zone. (a) Spectrum along Γ-K. (b) Spectrum in a direction perpendicular to Γ-K, along which the both branches of the π band are symmetric. Dashed lines are guides to the eye, with slope corresponding to a Fermi velocity of 10^6 m/s.

A weak coupling of graphene to the Pt(111) substrate, as indicated by the growth characteristics, the existence of different rotational alignments and interface structures, and an interlayer spacing close to that of graphite, should also be reflected in the electronic structure of the graphene monolayer. For strongly interacting systems, such as ML graphene on Ru(0001), the coupling to metal d states lifts the characteristic linear dispersion near the Fermi energy (E_F) in the interfacial graphene sheet.[30,31] Only the outer layer in bilayer graphene on Ru recovers a linear dispersion of π bands crossing E_F. For graphene on weakly interacting transition metals, such as Ir(111), Dirac cones have been observed already in the first monolayer.[44] This system also showed a significant modulation of the electrostatic potential across the graphene/Ir moiré, giving rise to a lateral superlattice in the ML graphene sheet. To probe the electronic structure of ML graphene on Pt(111), we have measured micro-ARPES band maps on individual monocrystalline graphene domains.

Figure 5 shows a comparison of micro-ARPES maps of the occupied bands at energies within 16 eV of E_F, for a large ML graphene domain on Pt(111) [Fig. 5(a)] and for exposed Pt(111) between graphene sheets [Fig. 5(b)]. The band structure of the graphene terminated area shows sharp bands with significant dispersion throughout the BZ. Comparison with scaled bands of free-standing graphene, calculated by DFT,[45] demonstrates an excellent overall match between these bands and the π and σ bands of isolated graphene. The additional ARPES intensity in Fig. 5(a) is entirely due to (111)-projected bands of the metal substrate, as demonstrated by the reference spectrum shown in Fig. 5(b). The observed bands in areas of exposed metal agree well with DFT calculations of the Pt(111) projected band structure.[46] In particular, our data show a high density of states at E_F and at about −4 eV at Γ, a continuum of bands at M, and a lower state density along with several projected

gaps at K. The difference between the Pt(111) derived bands with and without ML graphene is negligible, confirming the absence of any significant hybridization of graphene π states with metal d states. Hence, the ARPES band map of Fig. 5(a) essentially represents a superposition of graphene and metal-derived states, with minimal interaction between the two.

Figure 6 shows close-up ARPES maps of the graphene π band near the **K** point of the BZ close to the Fermi energy, along **Γ-K** [Fig. 6(a)], and in a direction perpendicular to **Γ-K** [Fig. 6(b)] in which both branches of the band are symmetric.[47] The measurement shows a linear π-band dispersion with Fermi velocity close to 10^6 m/s, as expected for free-standing graphene. However, the charge-neutrality ("Dirac") point lies above E_F, i.e., the ML graphene is hole doped by charge transfer from the substrate. Extrapolation of the linear π-band dispersion, measured within 2 eV below the Fermi level, gives an estimated band crossing at (0.30 ± 0.15) eV above E_F. This level of hole doping agrees well with a recent DFT calculation of the band structure of graphene on Pt(111), which has predicted the Dirac point about 0.3 eV above E_F.[48] Several additional micro-ARPES measurements on different ML graphene domains have shown no significant changes in the band structure and Dirac point energy as a function of interface registry. In particular, the graphene domains with large and small moiré unit cells [e.g., Figs. 3(a) and 3(b)] have identical band structure and hole doping.

IV. FEW-LAYER GRAPHENE ON Pt(111)

If sufficient interstitial carbon is available in the Pt substrate, the graphene growth by carbon segregation ultimately leads to the coalescence of the different graphene domains to form a complete layer covering the entire substrate surface, as verified by a LEEM survey of macroscopic sample areas. At this point (i.e., about 1 ML graphene coverage) the growth by segregation terminates. No nucleation and growth of additional graphene sheets are observed in areas covered by monocrystalline graphene domains. The only places where additional growth occurs are domain boundaries between graphene sheets with large rotational misalignment. A particularly striking example is shown in Fig. 7, a sequence of LEEM images illustrating the coalescence of three differ-
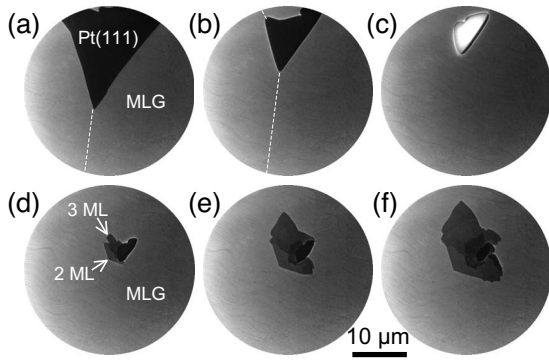
FIG. 7. Inhibited coalescence of ML graphene and nucleation of a few-layer graphene stack. [(a) and (b)] Coalescence of three misaligned ML graphene domains. Dashed lines denote the approximate location of the domain boundaries (identified from earlier frames of this LEEM movie). Temperature $T = 780\ ^\circ$C. (c) Inhibited coalescence and formation of a distinct surface phase with low work function in the remaining Pt(111) area not covered by graphene. $T = 780\ ^\circ$C. [(d)–(f)] Growth of a few-layer graphene stack near the uncovered area (temperatures: 750, 720, and 670 $^\circ$C, respectively).

ent ML graphene domains. While carbon incorporation into the graphene edges initially leads to the rapid advance of the edges of the different domains, the growth slows down progressively as the area of exposed Pt(111) shrinks. A finite area, several μm^2 in size, remains that does not become covered by graphene during further cooling and carbon surface segregation. At sufficiently high temperatures, the formation of a new surface phase in this pinhole is revealed by a sudden increase in the local electron intensity. From the temperature dependence of the electron intensity, we conclude that this effect is due to thermionic emission of electrons from the pinhole, indicating the formation of a surface phase with dramatically reduced work function. A complete identification of the structure and composition of this phase has proven elusive in our experiments to date. A possible scenario is the formation of a mixed Pt-C phase, perhaps with carbidic (instead of graphitic) binding, at very high carbon supersaturations made possible by the continued surface segregation and suppression of carbon incorporation into the existing graphene sheets.

In the vicinity of the remaining, stable pinhole in the ML graphene layer, additional segregating carbon can reach the surface and nucleate a few-layer graphene stack [Figs. 7(d)–7(f)] with thickness up to 10 layers or more. The observation of such additional growth exclusively at graphene grain boundaries or pinholes demonstrates two key characteristics governing graphene growth on Pt(111) and possibly other weakly interacting transition metals. First, no nucleation of further graphene layers occurs between an existing ML graphene sheet and the metal substrate, i.e., despite the weak coupling of the graphene sheet to the metal there is no interfacial growth mechanism that could lead to graphene structures with thickness beyond 1 ML. And second, ML graphene appears to be essentially impenetrable to carbon segregating from interstitial sites in the Pt bulk. Thus, a structurally coherent graphene sheet effectively prevents the

segregating carbon from reaching the surface. This latter finding is consistent with recent experiments on freestanding graphene membranes, which have concluded that monolayer graphene is impenetrable even to He atoms.[6] In the context of graphene growth on weakly interacting transition metals, it implies that an existing ML graphene sheet represents an effective diffusion barrier, which prevents continued carbon segregation to the surface and causes a self-termination of the growth at 1 ML graphene coverage.[33]

Graphene stacks formed near grain boundaries and coalescence zones can be used to obtain further information on the interlayer spacing in few-layer graphene on Pt(111). The morphology of these stacks is such that the thickness increases in monolayer steps from 1 ML graphene at the periphery toward thicker few-layer graphene at the center [Fig. 8(a)]. *IV*-LEEM spectra of the low-energy (2–100 eV) electron reflectivity for thicknesses between 1 and 10 graphene sheets are shown in Figs. 8(b) and 8(c). The *IV* curve for ML graphene is clearly distinct and reflects the 3.30 Å interfacial layer spacing discussed above. The spectra for stacks of multiple graphene sheets appear similar to one another at energies above 15 eV but are quite different at lower energies. Here, pronounced oscillations in the reflectivity are observed and the number of minima of these oscillations in the energy range shown in Fig. 7(c) scales with the number of graphene layers, similar to previous observations for graphene on SiC.[49] Further analysis clearly identifies these oscillations as fringes due to the interference of electrons backscattered at the surface of the graphene stack and at the graphene/Pt(111) interface. Similar quantum-size effects have been observed for heteroepitaxial thin films on metal substrates, e.g., Ag or Cu on W(110).[50,51] A phase accumulation model, analogous to that used for metallic thin films, can be employed to analyze this interference phenomenon. Assuming a free-electron dispersion in the graphene stack, the phase shift between the two interfering electron waves can be written as[51,52] $\phi = (\frac{2t}{\hbar})\sqrt{2m(E+V_0)}$, where E denotes the incident electron energy, V_0 the inner potential of the few-layer graphene stack, and t its thickness. Interference modulates the reflected intensity as a function of electron energy and film thickness (i.e., number of graphene layers). Phase shifts of even (odd) multiples of π give rise to constructive (destructive) interference, i.e., maxima (minima) in the electron reflectivity.

By plotting the phase shift, ϕ, as a function of the energies at which interference maxima or minima are observed, the local thickness of the graphene film can be determined precisely via a fit to the above expression. In practice, we find that each increase in film thickness by one graphene sheet gives rise to one additional interference minimum in the energy range between 2 and 15 eV, making it possible to determine the local film thickness by simply counting the interference minima. Figure 8(d) shows a summary of the energy-dependent phase shifts for three-layer to nine-layer graphene on Pt(111), based on the interference fringes shown in Fig. 8(c). Also shown in Fig. 8(d) are fits to these phase shifts, assuming free-electron dispersion. In contrast to quantum-size effects in metal films, for which the free-electron assumption is clearly violated,[51] we find excellent agreement with the free-electron model for few-layer
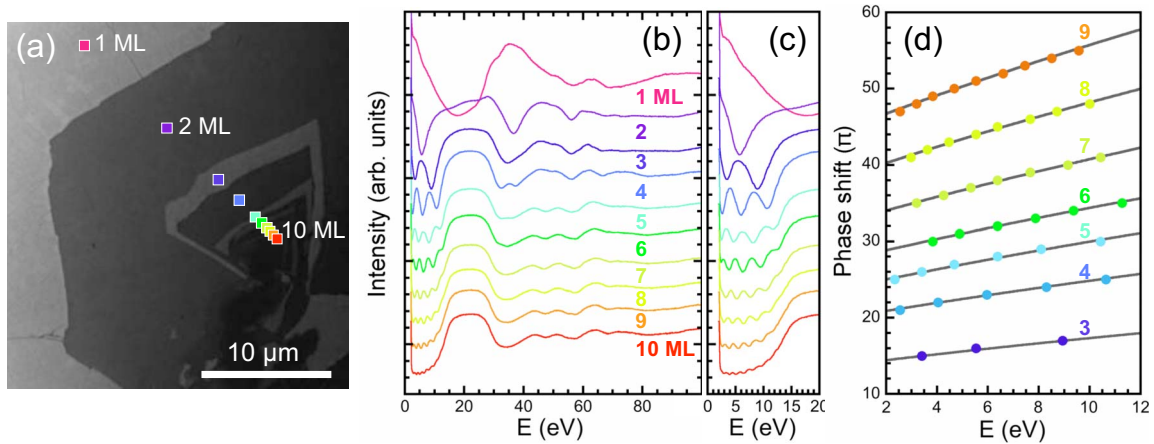
FIG. 8. (Color online) *IV* LEEM on few-layer graphene on Pt(111). (a) LEEM image (electron energy 4.4 eV) of a few-layer graphene stack nucleated at a boundary between rotationally misaligned ML graphene domains. Markers denote areas with coverage between 1 and 10 graphene layers. (b) *IV* characteristics obtained from a stack of LEEM images with electron energy from 2 to 100 eV at the locations marked in (a). (c) Higher magnification of the same data set at electron energies below 20 eV, showing fringes due to interference of electrons backscattered from the graphene surface and graphene/Pt interface. (d) Phase shifts for constructive and destructive interference [fringe maxima and minima in (c)] as a function of electron energy. Full lines are fits assuming free-electron like propagation.

graphene on Pt(111) if we assume an inner potential of -17 eV—close to the values derived for graphite by other measurements.[53] The fits are based on $m = m_e$, i.e., free-electron-like propagation and a thickness of an n-layer stack of $(n-1)d_G$, where $d_G = 0.335$ nm is the c-axis layer spacing in graphite. The quantum-size effect hence confirms that for stacks of 3 or more graphene layers, the separation between adjacent graphene is identical to the layer spacing in graphite.

V. CONCLUSIONS

To identify promising substrates for large-scale graphene synthesis, it is important to understand the substrate interaction—giving rise to characteristic growth, structural, and electronic properties—for graphene on different transition metals. We have used *in situ* observations of the growth and relaxation by wrinkle formation, along with measurements of the interface moiré structure, metal-graphene separation, and band structure, to examine the interaction between monolayer graphene and Pt(111). Low-energy electron microscopy of the graphene growth process shows the signatures of a weak metal-graphene interaction, in particular a minimal difference in the growth rate in the uphill and downhill directions across substrate steps. Other characteristics, such as a strong faceting of the edges of graphene domains over large distances, the facile formation of wrinkles in the graphene sheets to relax thermal stress, and the generation of a wide variety of rotational moiré variants, are consistent with a weak coupling of monolayer graphene to the Pt substrate. The different rotational alignments between graphene and Pt(111) give rise to two distinct families of moiré structures with large and small unit cells, respectively. In contrast to other systems—notably graphene on Ir(111)—none of these structures appears strongly preferred over the others, suggesting minor differences in energy between the various moirés. The growth rates of the two families of moiré struc-

tures show measurable differences, indicating that the growth kinetics are affected by the orientation of the initial graphene nuclei.

IV characteristics in microdiffraction, combined with *IV* simulations for a simplified (commensurate) structure have been used to determine the separation between monolayer graphene and the Pt(111) surface. Given a weak coupling and assuming a simple graphene-Pt interface, one might expect a separation close to the interlayer spacing in graphite. A previous report instead suggested the formation of a complex interface structure comprising a carbidic interlayer between graphene and Pt(111).[19] However, none of the other systems of graphene on transition metals appears to form such a complex interface. Our combined measurements and simulations lend additional support to the notion of a simple graphene-Pt interface and in this case give a separation (3.30 Å) that indeed lies close to the c-axis spacing in graphite. This finding suggests that the binding of graphene on Pt(111) may be understood in a common framework with other graphene-metal interfaces.

Direct evidence for a weak coupling between monolayer graphene and Pt(111) is provided by micro-APRES maps of the band structure. Apart from some residual hole doping due to charge transfer with the substrate, the electronic structure of monolayer graphene on Pt(111) is close to that of isolated graphene. In particular, the linear dispersion of π bands in the so-called Dirac cones, which gives rise to many exotic manifestations of massless Dirac fermions is preserved.

Finally, the near isolation of monolayer graphene on Pt(111) causes the self-termination of graphene growth by carbon segregation at a maximum coverage of 1 ML, due to the impermeability of structurally coherent graphene sheets to carbon diffusion, analogous to that observed for freestanding graphene.[6] The coalescence of different rotational graphene domains, however, can give rise to domain boundaries—the two-dimensional analog of a grain boundary in a polycrystalline thin film—that allow segregating car-

bon to reach the surface and to nucleate thicker few-layer graphene stacks. While for practical applications in large-scale graphene synthesis both the resulting structural defects and the uncontrolled thickness fluctuations at domain boundaries are undesirable, they enabled us to study the properties of few-layer graphene and will make it possible to investigate the physics of defect formation between misaligned graphene sheets.

[1] A. K. Geim and K. S. Novoselov, Nature Mater. **6**, 183 (2007).

[2] K. S. Novoselov, A. K. Geim, S. V. Morozov, D. Jiang, M. I. Katsnelson, I. V. Grigorieva, S. V. Dubonos, and A. A. Firsov, Nature (London) **438**, 197 (2005).

[3] S. V. Morozov, K. S. Novoselov, M. I. Katsnelson, F. Schedin, D. C. Elias, J. A. Jaszczak, and A. K. Geim, Phys. Rev. Lett. **100**, 016602 (2008).

[4] X. Wang, L. Zhi, and K. Mullen, Nano Lett. **8**, 323 (2008).

[5] F. Schedin, A. K. Geim, S. V. Morozov, E. W. Hill, P. Blake, M. I. Katsnelson, and K. S. Novoselov, Nature Mater. **6**, 652 (2007).

[6] J. S. Bunch, S. S. Verbridge, J. S. Alden, A. M. van der Zande, J. M. Parpia, H. G. Craighead, and P. L. McEuen, Nano Lett. **8**, 2458 (2008).

[7] P. W. Sutter, J.-I. Flege, and E. A. Sutter, Nature Mater. **7**, 406 (2008).

[8] A. T. N'Diaye, S. Bleikamp, P. J. Feibelman, and T. Michely, Phys. Rev. Lett. **97**, 215501 (2006).

[9] A. Reina, X. Jia, J. Ho, D. Nezich, H. Son, V. Bulovic, M. S. Dresselhaus, and J. Kong, Nano Lett. **9**, 30 (2009).

[10] K. S. Kim, Y. Zhao, H. Jang, S. Y. Lee, J. M. Kim, K. S. Kim, J.-H. Ahn, P. Kim, J.-Y. Choi, and B. H. Hong, Nature (London) **457**, 706 (2009).

[11] Q. Yu, J. Lian, S. Siriponglert, H. Li, Y. P. Chen, and S.-S. Pei, Appl. Phys. Lett. **93**, 113103 (2008).

[12] L. G. De Arco, Y. Zhang, A. Kumar, and C. Zhou, IEEE Trans. Nanotechnol. **8**, 135 (2009).

[13] S. Marchini, S. Gunther, and J. Wintterlin, Phys. Rev. B **76**, 075429 (2007).

[14] X. Li, W. Cai, J. An, S. Kim, J. Nah, D. Yang, R. Piner, A. Velamakanni, I. Jung, E. Tutuc, S. K. Banerjee, L. Colombo, and R. S. Ruoff, Science **324**, 1312 (2009).

[15] R. Rosei, S. Modesti, F. Sette, C. Quaresima, A. Savoia, and P. Perfetti, Phys. Rev. B **29**, 3416 (1984).

[16] A. Y. Tontegode, Prog. Surf. Sci. **38**, 201 (1991).

[17] B. Lang, Surf. Sci. **53**, 317 (1975).

[18] A. B. Preobrajenski, M. L. Ng, A. S. Vinogradov, and N. Martensson, Phys. Rev. B **78**, 073401 (2008).

[19] H. Zi-Pu, D. F. Ogletree, M. A. Van Hove, and G. A. Somorjai, Surf. Sci. **180**, 433 (1987).

[20] T. A. Land, T. Michely, R. J. Behm, J. C. Hemminger, and G. Comsa, Surf. Sci. **264**, 261 (1992).

[21] M. Enachescu, D. Schleef, D. F. Ogletree, and M. Salmeron, Phys. Rev. B **60**, 16913 (1999).

[22] M. Sasaki, Y. Yamada, Y. Ogiwara, S. Yagyu, and S. Yamamoto, Phys. Rev. B **61**, 15653 (2000).

[23] D. E. Starr, E. M. Pazhetnov, A. I. Stadnichenko, A. I. Boronin, and S. K. Shaikhutdinov, Surf. Sci. **600**, 2688 (2006).

[24] E. Loginova, S. Nie, K. Thurmer, N. C. Bartelt, and K. F. McCarty, Phys. Rev. B **80**, 085430 (2009).

[25] R. H. Siller, W. A. Oates, and R. B. McLellan, J. Less-Common Met. **16**, 71 (1968).

[26] J. I. Flege, J. Hrbek, and P. Sutter, Phys. Rev. B **78**, 165407 (2008).

[27] V. Blum and K. Heinz, Comput. Phys. Commun. **134**, 392 (2001).

[28] J. I. Flege, E. Vescovo, G. Nintzel, L. H. Lewis, S. Hulbert, and P. Sutter, Nucl. Instrum. Methods Phys. Res. B **261**, 855 (2007).

[29] J. Coraux, A. T. N'Diaye, C. Busse, and T. Michely, Nano Lett. **8**, 565 (2008).

[30] T. Brugger, S. Günther, B. Wang, H. Dil, M.-L. Bocquet, J. Osterwalder, J. Wintterlin, and T. Greber, Phys. Rev. B **79**, 045407 (2009).

[31] P. Sutter, M. S. Hybertsen, J. T. Sadowski, and E. Sutter, Nano Lett. **9**, 2654 (2009).

[32] E. A. Sutter, D. P. Acharya, and P. W. Sutter, Appl. Phys. Lett. **94**, 133101 (2009).

[33] J. Coraux, A. T. N'Diaye, M. Engler, C. Busse, D. Wall, N. Buckanie, F. J. Meyer zu Heringdorf, R. van Gastel, B. Poelsema, and T. Michely, New J. Phys. **11**, 039801 (2009).

[34] A. N. Obraztsov, E. A. Obraztsova, A. V. Tyurnina, and A. A. Zolotukhin, Carbon **45**, 2017 (2007).

[35] L. B. Biedermann, M. L. Bolen, M. A. Capano, D. Zemlyanov, and R. G. Reifenberger, Phys. Rev. B **79**, 125411 (2009).

[36] Alpha T. N'Diaye, R. v. Gastel, A. J. Martinez-Galera, J. Coraux, H. Hattab, D. Wall, F.-J. M. z. Heringdorf, M. H.-v. Hoegen, J. M. Gomez-Rodriguez, B. Poelsema, C. Busse, and T. Michely, arXiv:0906.0896 (unpublished).

[37] W. S. Rasband and J. Image, Available at http://rsb.info.nih.gov/ij/ (U.S. National Institutes of Health, Bethesda, Maryland, USA, 1997–2009).

[38] R. Khare, S. L. Mielke, J. T. Paci, S. Zhang, R. Ballarini, G. C. Schatz, and T. Belytschko, Phys. Rev. B **75**, 075412 (2007).

[39] H. Ueta, M. Saida, C. Nakai, Y. Yamada, M. Sasaki, and S. Yamamoto, Surf. Sci. **560**, 183 (2004).

[40] B. Wang, M.-L. Bocquet, S. Marchini, S. Günther, and J. Wintterlin, Phys. Chem. Chem. Phys. **10**, 3530 (2008).

[41] A. T. N'Diaye, J. Coraux, T. N. Plasa, C. Busse, and T. Michely, New J. Phys. **10**, 043033 (2008).

[42] P. A. Khomyakov, G. Giovannetti, P. C. Rusu, G. Brocks, J. van den Brink, and P. J. Kelly, Phys. Rev. B **79**, 195425 (2009).

[43] Our measured *IV* characteristics differ significantly from those obtained previously (Ref. 19). This suggests that the different conclusions in the analysis of the graphene/Pt(111) interface are

not primarily due to the different approaches used in the LEED *IV* simulation but may result from different preparation (controlled carbon segregation versus room-temperature hydrocarbon adsorption and annealing) and measurement conditions (selected area micro-LEED *IV* versus area-averaged conventional LEED *IV*).

[44] I. Pletikosic, M. Kralj, P. Pervan, R. Brako, J. Coraux, A. T. N'Diaye, C. Busse, and T. Michely, Phys. Rev. Lett. **102**, 056808 (2009).

[45] C. Heske, R. Treusch, F. J. Himpsel, S. Kakar, L. J. Terminello, H. J. Weyer, and E. L. Shirley, Phys. Rev. B **59**, 4680 (1999).

[46] A. Kokalj and M. Causa, J. Phys.: Condens. Matter **11**, 7463 (1999).

[47] S. Y. Zhou, G. H. Gweon, A. V. Fedorov, P. N. First, W. A. de Heer, D. H. Lee, F. Guinea, A. H. Castro Neto, and A. Lanzara,

Nature Mater. **6**, 770 (2007).

[48] G. Giovannetti, P. A. Khomyakov, G. Brocks, V. M. Karpan, J. van den Brink, and P. J. Kelly, Phys. Rev. Lett. **101**, 026803 (2008).

[49] T. Ohta, F. E. Gabaly, A. Bostwick, J. L. McChesney, K. V. Emtsev, A. K. Schmid, T. Seyller, K. Horn, and E. Rotenberg, New J. Phys. **10**, 023034 (2008).

[50] W. F. Chung, Y. J. Feng, H. C. Poon, C. T. Chan, S. Y. Tong, and M. S. Altman, Phys. Rev. Lett. **90**, 216105 (2003).

[51] M. S. Altman, W. F. Chung, and C. H. Liu, Surf. Rev. Lett. **5**, 1129 (1998).

[52] B. T. Jonker, N. C. Bartelt, and R. L. Park, Surf. Sci. **127**, 183 (1983).

[53] S. Y. Zhou, G. H. Gweon, and A. Lanzara, Ann. Phys. **321**, 1730 (2006).